

On the Relative Importance of Motion-Related Contributions to the SAR Imaging Mechanism of Ocean Surface Waves

WERNER R. ALPERS AND CLAUS BRUENING

Abstract—The relative importance of the various motion-related contributions to the SAR imaging mechanism of ocean surface waves is studied by using two-dimensional Monte Carlo simulation techniques. It is shown that for wind waves the often-observed stretching of the peak wavelength and the rotation of the spectral peak toward the range direction is caused by both the degradation in azimuthal resolution and the nonlinearity of the velocity bunching mechanism. The distortion of the SAR image spectrum relative to the ocean wave spectrum due to the degradation in azimuthal resolution is mainly caused by the spread of the radial facet velocities within a SAR resolution cell. The effect of the radial orbital acceleration arising from the long waves of scales larger than a SAR resolution cell on the nonlinearity of the SAR imaging mechanism is small.

It is argued that the effect of the wave motions on the SAR imaging mechanism cannot always be reduced to a linear azimuthal low-pass filter acting on the ocean slope spectrum. In those cases where the imaging is nonlinear, the ocean wave spectrum cannot be retrieved from the SAR image spectrum by applying linear inversion techniques. For swell imaging, the nonlinearities are usually less strong because swell spectra have a narrower width than wind spectra.

Computer simulations of SAR imaging of fully developed wind seas with different peak wavelengths and propagation directions are presented.

I. INTRODUCTION

SYNTHETIC aperture radar (SAR) is a high-resolution imaging instrument flown on aircraft or spacecraft operating at microwave frequencies. When applied to imaging stationary flat surfaces, a properly designed SAR constitutes a linear imaging device [1], [2].

However, when applied to image ocean surface waves, SAR may turn into a nonlinear imaging system. This is because SAR obtains its fine resolution in flight (or azimuth) direction by using the phase history of the backscattered signal. Sea surface motions distort the expected stationary target phase history and thus affect the imaging process in azimuth direction.

Though basically the SAR response to a moving ocean

wave field seems now well understood (see [3] for a review), there is still considerable discussion on the relative importance of motion effects on spatial scales larger and smaller than the SAR resolution cell. Still a controversial issue is how the scatterer velocities and accelerations on these two scales affect SAR image spectra. In particular, the following questions arise:

- 1) What is the physical reason for the often observed azimuth cutoff of SAR image spectra [4]–[7]?
- 2) Why is the peak of SAR image spectrum, when compared to the peak of the corresponding ocean wave spectrum, often shifted toward lower wavenumbers and rotated toward the range direction [8]?
- 3) Can the ocean wave spectrum be retrieved from the SAR image spectrum by applying linear inversion techniques even in those cases where the SAR imaging process leads to strongly distorted SAR image spectra? Are the motion-induced distortions always describable by a linear low-pass filter function [9]?

This paper aims at answering these questions. In Section II basic concepts of the SAR imaging mechanism of ocean surface waves are reviewed. The effect of the velocity spread of the scatter elements within a SAR resolution cell to the degradation in azimuthal resolution is discussed in Section III. In Section IV the SAR imaging mechanism of ocean surface waves is studied by using Monte Carlo simulation techniques. The relative importance of the various motion-related contributions to the SAR imaging process is investigated by turning off successively contributing terms in the imaging mechanism. The last section contains a discussion of the numerical simulation studies.

II. BASIC CONCEPTS OF THE SAR IMAGING THEORY

The effect of sea surface motions on SAR imagery of ocean surface waves has been investigated by a number of authors [10]–[26]. Most of these authors support the “floating cork” or moving facet model as the proper backscatter model of the sea surface for describing the SAR response to moving ocean surface waves. In this model the sea surface is represented by moving facets (“corks”) that have uncorrelated complex backscattering coefficients. The facets have dimensions that are large compared to the radar wavelength, but small compared to

Manuscript received August 25, 1985; revised April 23, 1986. This work was supported by the Deutsche Forschungsgemeinschaft (SFB 94, Meeresforschung Hamburg), the Bundesministerium fuer Forschung und Technologie, and the Office of Naval Research under Grant N 00014-83-G-0126, monitored by H. Dolezalek.

W. R. Alpers is with the Universitaet Bremen, Fachbereich Physik/Elektrotechnik, 2800 Bremen 33, Federal Republic of Germany.

C. Bruening is with the Max-Planck-Institut fuer Meteorologie, 2000 Hamburg 13, Federal Republic of Germany.

IEEE Log Number 8610376.

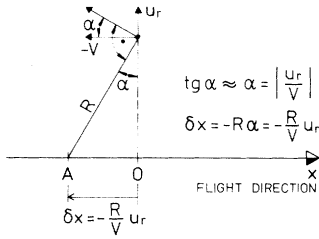


Fig. 1. Derivation of the azimuthal displacement δx of a moving target in the SAR image. SAR positions the target in azimuth at zero-Doppler, which for a stationary target is at broadside (point 0), and for a target with radial velocity component u_r , at $\delta x = -(R/V)u_r$ off broadside (point A).

the wavelength of the long surface waves to be imaged by the radar. The motion of the facets is determined by the orbital motion associated with the long surface waves. The orbital motions lead to azimuthal displacements of the facets in the image plane and to azimuthal image smear. The azimuthal displacement is caused by the facet velocity in look direction of the antenna (range direction).

If a target has a velocity component direction u_r in range direction, then zero Doppler of the backscattered signal originating from this target is not encountered exactly at broadside, i.e., at right angles to the flight path, but at an angle $\alpha \approx \text{tg} \alpha = |u_r/V|$ off-broadside as shown in Fig. 1. Here, V denotes the platform velocity. A SAR that is tuned for stationary targets positions a target in azimuth at zero Doppler. However, if a scattering element has a velocity component u_r in range direction, then its SAR image is displaced in azimuth (the x -direction) by the amount

$$\delta x = -(R/V)u_r \quad (1)$$

relative to the image of a stationary scattering element. Here, R denotes the range or distance between the SAR antenna and the target. Ample evidence of this effect can be found in SAR imagery containing moving objects. For example, trains or ships having velocity components in range direction, are displaced in azimuth direction relative to their tracks or wakes, respectively.

The spatially variable facet velocities associated with the orbital velocities of the long ocean surface waves give rise to alternating concentration and spreading of the position of the facets. This is the so-called "velocity bunching effect," which contributes to the SAR imaging mechanism of ocean surface waves [19].

In this SAR imaging theory, which is sometimes also called "velocity bunching theory," the phase velocity of the long ocean waves does not enter.

Very convincing experimental confirmation of the velocity bunching effect has recently been reported by Lyzenga *et al.* [26] who investigated SAR imagery of ocean waves propagating in open water and ice. They show a SAR image intensity profile of waves traveling in ice, which has exactly the strongly nonsinusoidal form as predicted by the velocity bunching theory [11]–[13], [16], [17], [19]. The SAR image intensity spectrum also clearly

exhibits the theoretically expected first harmonic of the dominant wave component.

Velocity bunching often constitutes an inherent nonlinear contribution to the SAR imaging mechanism of ocean surface waves. Only in a limited range of ocean wave/SAR parameters can it be approximated by a linear process [3], [19]. One of the principle goals of this paper is to point out that linear system theory is often inadequate to establish the relationship between SAR image and ocean wave spectra. In particular, this applies to Seasat SAR [27] and the SAR on board the future European Remote Sensing Satellite ERS-1 [28] when imaging wind waves that propagate at a substantial angle off the range direction.

Velocity bunching is not the only effect by which the motion of the ocean surface enters into the SAR imaging mechanism. The orbital acceleration arising from the long waves of a scale larger than the SAR resolution cell and the spread of the facet velocities within a SAR resolution cell cause a degradation of the azimuthal resolution. The expression for the degraded azimuthal resolution for N incoherent looks ρ'_{aN} reads [16], [19], [20]

$$\rho'_{aN}(x) = \left[\rho_{aN}^2 + \left(\frac{\pi}{2} (R/V) \hat{a}_r(x_0) T \right)^2 + \left(\rho_a \frac{T}{\tau_s} \right)^2 \right]^{1/2} \quad (2)$$

where

$$\rho_a = \lambda_0 R / 2VT \quad (3)$$

is the full-bandwidth azimuthal SAR resolution, $\rho_{aN} = N\rho_a$, λ_0 the radar wavelength, T the full-bandwidth SAR coherent integration time, $\hat{a}_r(x_0)$ the radial orbital acceleration arising from the long waves of scale larger than the SAR resolution cell, and τ_s a scene coherence time that is primarily determined by the spread of the facet velocities within a SAR resolution cell. The physical origin of the scene coherence time will be discussed in detail in the next section.

Note that the last term in (2) is independent of the space variable $x_0 = (x_0, y_0)$, while the second term is a function of the position on the long wave profile. The last term originates from a random process and causes a constant azimuthal image smear, while the second term is deterministically related to the long ocean wave field and causes a spatially variable azimuthal image smear. If this second term were missing in (2), the degradation in azimuthal resolution would result in an azimuthal low-pass filter acting on the wave spectrum. Both terms lead to a degradation in azimuthal resolution. They are both proportional to R/V (as can be seen by inserting (3) into (2)), but independent of the number of incoherent looks. Furthermore, the acceleration term arising from the long waves depends on integration time T , while the term containing the scene coherence time τ_s does not depend on T .

According to velocity bunching theory, the ensemble-averaged SAR image intensity distribution $I(x, y)$ generated by a moving ocean wave field $\hat{\zeta}(x_0, y_0)$ is given by [11], [19], [20].

$$I(x, y) = B \int_{-\infty}^{\infty} dx_0 dy_0 \sigma(x_0) \Delta(y - y_0) \times \exp \left\{ -\frac{\pi^2}{\rho_{aN}^2(x_0)} [x - x_0 - (R/V) \hat{u}_r(x_0)]^2 \right\} \quad (4)$$

Here $\hat{u}_r(x_0) = \hat{u}_r(x_0, y_0)$ denotes the radial component of the mean orbital velocity of an ocean patch having the dimension of the SAR resolution cell, $\Delta(y)$ the SAR impulse response function in crosstrack (ground range) direction, and B a constant that depends on the system parameters of the SAR system, including the SAR correlator. $\sigma(x_0)$ is the ensemble-averaged normalized radar cross section that we assume to be linearly related to the waveheight $\hat{\zeta}(x_0)$ of the long wave field. The transfer function R between $\hat{\zeta}(x_0)$ and $\sigma(x_0)$ is assumed to be known and given by the sum of the tilt and hydrodynamic modulation transfer functions R^{tilt} and R^{hydr} , respectively [19], [3]

$$R^{\text{RAR}} = R^{\text{tilt}} + R^{\text{hydr}} \quad (5)$$

The superscript RAR in (5) indicates that it is this modulation that renders the long ocean waves detectable by real aperture radar (RAR).

Velocity bunching occurs if the gradient of $\hat{u}_r(x_0)$ in azimuth direction does not vanish, $(\partial/\partial x_0)\hat{u}_r(x_0) \neq 0$. Note that for $\hat{u}_r(x_0) = 0$ and $\hat{a}_r(x_0) = 0$ (4) is a convolution-type integral, but not for $\hat{u}_r(x_0) \neq 0$ and $\hat{a}_r(x_0) \neq 0$. However, for a certain range of nonvanishing ocean wave parameters, (4) can be approximated by such an integral as discussed in [19]. In this special case, velocity bunching can be approximated by a linear transfer function R^{vb} , and the total SAR modulation transfer function (MTF) then reads

$$R^{\text{SAR}} = R^{\text{RAR}} + R^{vb}. \quad (6)$$

Theory predicts that $|R^{\text{RAR}}|$ is proportional to $|k|$ and $|R^{vb}|$ proportional to $|k|^{3/2}$ [19].

In the case of linear imaging the relationship between the power spectrum of the ocean waveheight in a two-dimensional wave vector space, $P_{\hat{\zeta}}(k)$, and the power spectrum of the SAR image intensity, $P_I(k)$, is given by [5], [9]

$$P_I(k) = |G(k)|^2 |H(k_a)|^2 |R^{\text{SAR}}(k)|^2 P_{\hat{\zeta}}(k). \quad (7)$$

Here, $G(k)$ denotes the system transfer function, which is the Fourier transform of the SAR impulse response function for stationary targets, and $H(k_a)$ a low-pass filter function that affects only the azimuthal wave vector component k_a . The width of this low-pass filter is determined by the degraded azimuthal resolution. It depends mainly on the scene coherence time τ_s .

It was first pointed out by Raney [29] that a finite scene coherence time may be an important factor in the SAR imaging mechanism of ocean surface waves. It degrades the azimuthal resolution. Yet, it is not the only motion-induced effect, which causes a distortion of the SAR image intensity spectrum. The nonlinearity of velocity

bunching arising from the long waves of scales larger than the SAR resolution cell is also an important factor that enters into the SAR imaging mechanism of ocean waves. Often this nonlinearity contributes significantly to the distortion of the SAR image spectrum.

III. SCENE COHERENCE TIME

When investigating the SAR response to moving ocean waves, the authors of [16], [19], and [20] practically disregarded the effect of the finite scene coherence time on the imaging mechanism by choosing a large value for the scene coherence time. They associated the scene coherence time with the dynamic interaction time or "lifetime" of the Bragg waves, which is much larger than typical SAR integration times. Indeed, the effect of the scene coherence time on the imaging mechanism is probably small when the SAR resolution cell has the same dimension as a facet as defined in the two-scale wave model. However, for many SAR systems, e.g., the SAR's on board the Seasat and ERS-1 satellites, the SAR resolution cell is much larger than the facet size. The spatial dimensions of the facets are typically of the order of 10 to 20 Bragg wavelengths [3]. Therefore, in the case of a resolution cell comprising several facets, one has to take into account the Doppler spread of the backscattered signal caused by the motion of the facets within the resolution cell. This leads to an additional azimuthal image smear which can be expressed in terms of a scene coherence time τ_s .

The distribution of the facet velocities within a resolution cell can be assumed to be approximately Gaussian, independent of time and independent of the position on the long wave profile. The associated rms azimuthal image smear $\langle(\delta x)^2\rangle^{1/2}$ is therefore given by

$$\langle(\delta x)^2\rangle^{1/2} = (R/V)\langle u_r^2\rangle^{1/2} \quad (8)$$

where $\langle u_r^2\rangle^{1/2}$ is the rms radial facet velocity within a SAR resolution cell. Note that the facet accelerations do not lead to an additional contribution to the azimuthal image smear because of the time independence of the process, as shown in [3].

In the spectral domain, such azimuthal image smear corresponds to a low-pass filter, which acts on the azimuthal components of the SAR image intensity spectrum. This filter function has a Gaussian form and its width is inversely proportional to the rms azimuthal image smear $\langle(\delta x)^2\rangle^{1/2}$.

Assuming that the ocean wave spectrum can be described by a Pierson-Moskowitz spectrum [30] and that the ocean surface is viewed by the SAR under a small incidence angle θ ($\theta \approx 20^\circ$), we obtain approximately

$$\langle u_r^2\rangle \approx \langle u^2\rangle = \int_{\omega_1}^{\omega_2} d\omega \omega^2 \alpha g^2 \omega^{-5} \exp[-(\beta(g/U\omega)^4)] \quad (9)$$

where $\langle u^2\rangle^{1/2}$ is the rms facet velocity within a resolution cell, $\alpha = 0.0081$ the Phillips constant, g the acceleration

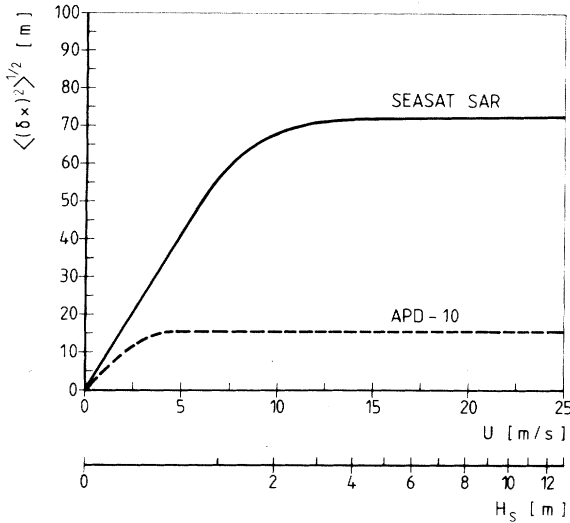


Fig. 2. Azimuthal image smear $\langle(\delta x)^2\rangle^{1/2}$ caused by the radial velocity spread within a resolution cell (see (11)) as a function of wind speed U and significant wave height H_s for fully developed wind seas. The upper curve applies for the spaceborne Seasat SAR system with a resolution of 25 m and $R/V = 128$ s, and the lower curve applies for the airborne APD-10 SAR system with 3-m resolution and $R/V = 80$ s.

of gravity, $\beta = 0.74$, U the windspeed at a height of 19.5 m, and $\omega = 2\pi f$ the radian frequency of the ocean waves. The lower limit of integration ω_1 is given by the frequency of the wave whose wavelength λ_1 is twice the geometric mean of the ground range and azimuth resolution [31]. By using the dispersion relation for water waves [30] we obtain

$$\omega_1 = [(2\pi g/\lambda_1) + \tau(2\pi/\lambda_1)^3]^{1/2}. \quad (10)$$

Here, τ denotes the surface tension of water, and λ_1 is given by

$$\lambda_1 = 2(\rho_a \rho_g)^{1/2} = 2\rho \quad (11)$$

where ρ_a is the processed azimuthal resolution and ρ_g the ground range resolution. This lower limit corresponds to the shortest resolvable wavelength that is determined by the Nyquist theorem. The upper limit of integration is determined by the facet size, but can, for computational convenience, be replaced by $\omega_2 = \infty$. The error introduced by this change in the integration limit is small. Inserting (9) into (8) and carrying out the integration yields [25]

$$\langle(\delta x)^2\rangle^{1/2} = (R/V) \left[\frac{\alpha}{4} \left(\frac{\pi}{\beta} \right)^{1/2} U^2 \operatorname{erf}(\gamma\rho/U^2) \right]^{1/2} \quad (12)$$

with

$$\gamma = \pi^{-1} g \beta^{1/2} = 2.69 \text{ m/s}^2.$$

Equation (12) is plotted in Fig. 2 as a function of U . For fully developed wind seas the wind speed U at a height of 19.5 m and the significant waveheight H_s are related by

$$U^2 = 47.4 H_s \quad (13)$$

if U is measured in meters per second and H_s in meters.

The upper curve applies for the SAR on board the Seasat satellite ($\rho = 25$ m, $R/V = 128$ s), and the second curve for the airborne X-band APD-10 system with $\rho = 3$ m and $R/V = 80$ s, which has been flown during the MARSEN 1979 experiment in the North Sea [6], [7].

Equation (12) simplifies for $\gamma\rho/U^2 \ll 1$ (high wind speed case) to

$$\langle(\delta x)^2\rangle^{1/2} = 11.24 \times 10^{-2} (R/V)\rho^{1/2} \quad (14)$$

which is independent of sea state, and for $\gamma\rho/U^2 \gg 1$ (low wind speed case) to

$$\begin{aligned} \langle(\delta x)^2\rangle^{1/2} &= 6.46 \times 10^{-2} (R/V)U \\ &= 0.44 (R/V)H_s^{1/2}. \end{aligned} \quad (15)$$

It follows from this equation that, for low wind speeds, the width of the azimuthal low-pass filter is proportional to $(V/R)H_s^{-1/2}$ (see (7)). This implies that the azimuthal cutoff wavenumber in the SAR image spectrum associated with the velocity spread of the facets within a SAR resolution cell is proportional to $(R/V)H_s^{1/2}$.

If we allow for a maximum error of 5 percent, then (14) applies already for $\gamma\rho/U^2 \leq 0.4$ and (15) for $\gamma\rho/U \geq 1.4$. In the case of Seasat SAR with $\rho = 25$ m, this means that (13) applies for wind speeds above 13 m/s and (15) for wind speeds below 7 m/s. Equation (14) yields in this case $\langle(\delta x)^2\rangle^{1/2} = 73$ m and (15), e.g., for $U = 3$ m/s, $\langle(\delta x)^2\rangle^{1/2} = 25$ m. From the last example we conclude that the effect of the azimuthal image smear $\langle(\delta x)^2\rangle^{1/2}$ on the imaging mechanism is small when SAR images swell in the presence of low local winds.

Conventionally the stationary target azimuthal SAR impulse response function is defined by

$$g(x) = \pi^{1/2} \rho_{aN}^{-1} \exp[-\pi^2 x^2 / \rho_{aN}^2]. \quad (16)$$

The spread of the facet velocities within a resolution cell causes an additional broadening of the stationary target impulse response function, which can be calculated by convolving $g(x)$ with

$$h(x) = 2\pi \langle(\delta x)^2\rangle^{-1/2} \exp[-x^2 / 2\langle(\delta x)^2\rangle]. \quad (17)$$

The result is an impulse response function with a width of

$$\rho'_{aN} = [\rho_{aN}^2 + 2\pi^2 \langle(\delta x)^2\rangle]^{1/2}. \quad (18)$$

The relationship between the azimuthal image smear due to the spread of the facet velocities within a resolution cell and the scene coherence time τ_s is given by [6], [26] (see (2))

$$2\pi^2 \langle(\delta x)^2\rangle = \rho_a \left(\frac{T}{\tau_s} \right)^2 = \left(\frac{R\lambda_0}{2V\tau_s} \right)^2 \quad (19)$$

yielding

$$\begin{aligned} \tau_s &= (2\pi \sqrt{2})^{-1} (R/V) \lambda_0 \langle(\delta x)^2\rangle^{-1/2} \\ &= (2\pi \sqrt{2})^{-1} \lambda_0 \langle u_r^2 \rangle^{-1/2}. \end{aligned} \quad (20)$$

Therefore, (18) can also be written as

$$\rho'_{aN} = \left[\rho_{aN}^2 + \left(\frac{R\lambda_0}{2V\tau_s} \right)^2 \right]^{1/2} \quad (21)$$

with τ_s given by (20).

The coherence time τ_s defined by (20) is related to the decorrelation time τ_D of Tucker [31] by

$$\tau_s = (\ln 2)^{-1/2} \tau_D = 1.2 \tau_D. \quad (22)$$

Tucker has defined the decorrelation time τ_D as the point where the envelope of the autocovariance function of the backscattered signal has dropped from its maximum value by 3 dB.

Applied to Seasat SAR we obtain from (20) with $\lambda_0 = 0.235$ m for $U > 13$ m/s (see (14))

$$\tau_s = 0.047 \text{ s}. \quad (23)$$

and for $U = 3$ m/s (see (14))

$$\tau_s = 0.14 \text{ s}. \quad (24)$$

These scene coherence times are considerably smaller than the one cited in [16], [19], and [20], which are of the order of several seconds. The reason for this is that in these papers no distinction was made between the electromagnetic-hydrodynamic two-scale model and the SAR-two-scale model. That these two models are not identical for many SAR systems, including Seasat SAR, has been discussed in detail in [3]. For Seasat SAR the scene coherence time is not primarily determined by the internal dynamics of the Bragg waves, i.e., by the dynamic interaction time or "lifetime" of the Bragg waves, but rather by the variability of the individual facet velocities within a SAR resolution cell. The Doppler width associated with this velocity spread of the intermediate-scale waves leads to scene coherence times that are much smaller than the dynamic interaction time of the Bragg waves.

The actual scene coherence time may, in some cases, be even smaller than the values calculated above. This is expected in particular for high sea states when non-Bragg scattering processes such as specular reflection and wedge scattering from breaking and cusping waves become important. [3].

IV. TWO-DIMENSIONAL MONTE CARLO SIMULATIONS

The relative importance of velocity bunching, degradation of azimuthal resolution due to orbital acceleration arising from the long waves of scale larger than the SAR resolution cell and due to the spread of the facet velocities within a resolution cell, can be studied by simulating the SAR imaging mechanism of moving ocean waves on a computer.

The method consists in generating first a realization of a two-dimensional wave field with a given spectrum by using the Monte Carlo method and then applying the SAR imaging mechanism as described by (4). In the present simulation study we have used the Seasat parameters ($R/V = 128$ s, $\lambda_0 = 0.235$ m, $\rho_a = 6.25$ m, $N = 4$, ρ_{aN}

$= 25$ m). From the resulting two-dimensional image intensity field the instantaneous SAR image spectrum is calculated. In the simulation study described here one realization of the ocean scene covers an area of $3.2 \text{ km} \times 3.2 \text{ km}$. The pixel separation is 25 m. Therefore, the resulting two-dimensional array consists of 128×128 data points. Fifty different simulation runs are performed for a given set of ocean wave and radar parameters such that the resulting simulated spectra have 100 degrees of freedom.

This two-dimensional Monte Carlo simulation study is an extension of a previously reported one-dimensional study to which the reader is referred for details [20]. The present investigation was carried out on an array processor (FPS 100/VAX). Several hundred simulation runs with a wide range of radar/ocean wave parameters were performed. The results of this systematic investigation will be presented elsewhere. Here we discuss only those basic features of the imaging mechanism that are still discussed controversially in the literature.

The effect of the three motion-related contributions on the SAR imaging mechanism is illustrated by two examples shown in Figs. 3 and 4. In these examples the SAR imaging of a fully developed wind sea of 219-m peak wavelength traveling at zero and 45 degrees to the flight direction, respectively, is studied. The ocean wave spectrum is modeled by a Pierson-Moskowitz spectrum [30] with a frequency-dependent angular spreading function as proposed by Mitsuyasu *et al.* [32]. Fig. 3(a) and Fig. 4(a) show the ocean waveheight spectra in wavenumber space as obtained from 50 Monte Carlo runs. In order to get an insight into the relative importance of the three motion-induced contributions to the imaging mechanism, the SAR image intensity spectra are calculated from ocean wave spectra by applying different combinations of the three contributions. The imaging is studied by using the Seasat SAR parameters.

In these examples we have modeled the sum of the tilt and hydrodynamic MTF (RAR MTF) by

$$|R^{\text{RAR}}| = 2.5 (1 + |\sin \phi|) |k| \quad (25)$$

$$\text{phase } \{R^{\text{RAR}}\} = 45^\circ \times \sin \phi$$

where ϕ is the angle between the wave propagation and the flight direction ($\phi = 0^\circ$ for azimuthally traveling waves and k the wave vector of the long waves). R^{RAR} is largest for range traveling waves ($\phi = 90^\circ$) and smallest for azimuthal traveling waves. Such MTF would yield, if applied to real aperture radar imaging of ocean surface waves, a radar image intensity spectrum that is proportional to the ocean slope spectrum $|k|^2 P_\xi(k)$. However, for the cases of ocean wave imaging by Seasat SAR considered in this paper, the specific value and the functional dependence of the RAR MTF are, if chosen within the experimental limits, not crucial, since the motion-induced contributions dominate the imaging process.

In all Monte Carlo runs presented in this paper the contribution from the tilt and hydrodynamic modulation is always included. Fig. 3(b) and Fig. 4(b) show the simu-

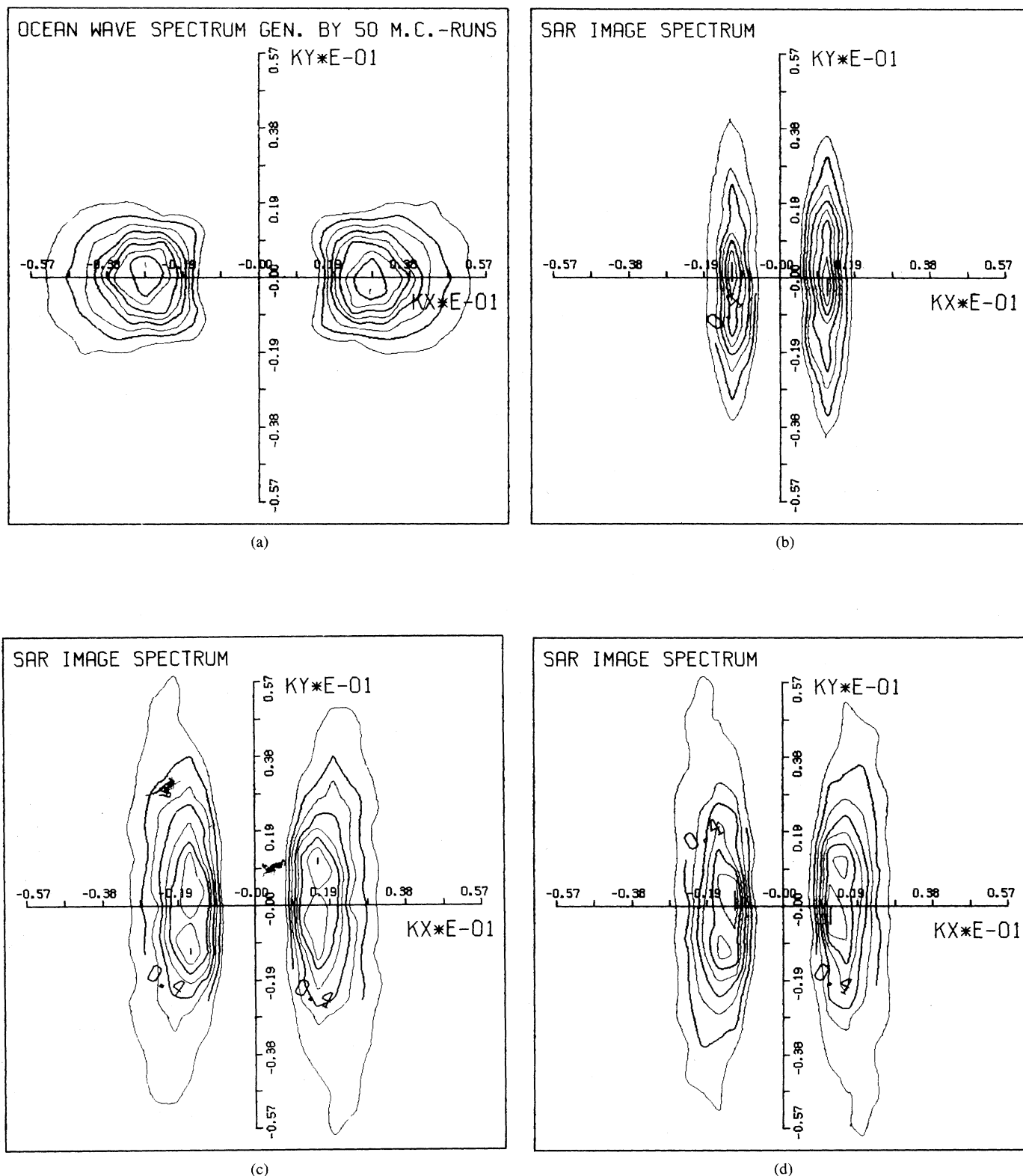
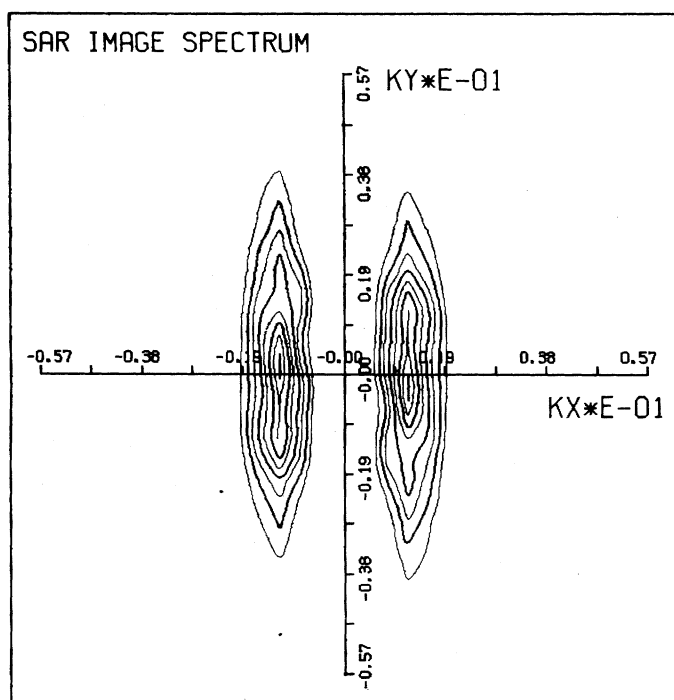
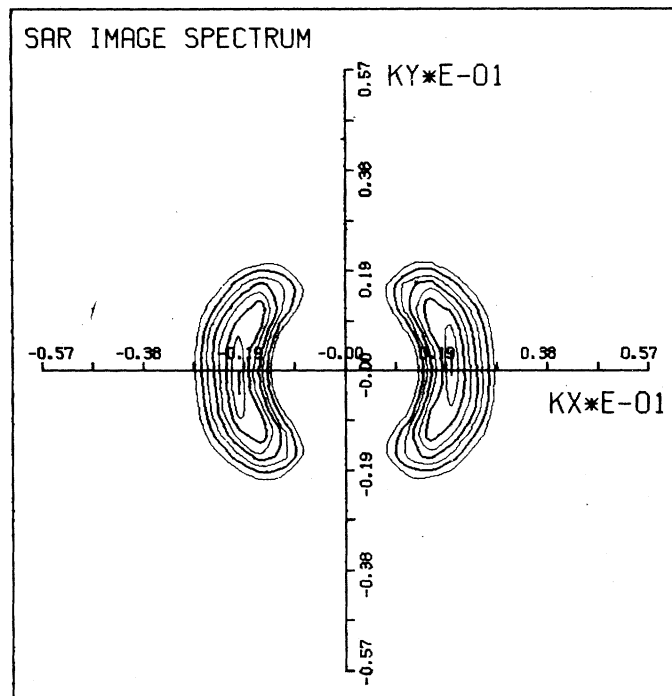


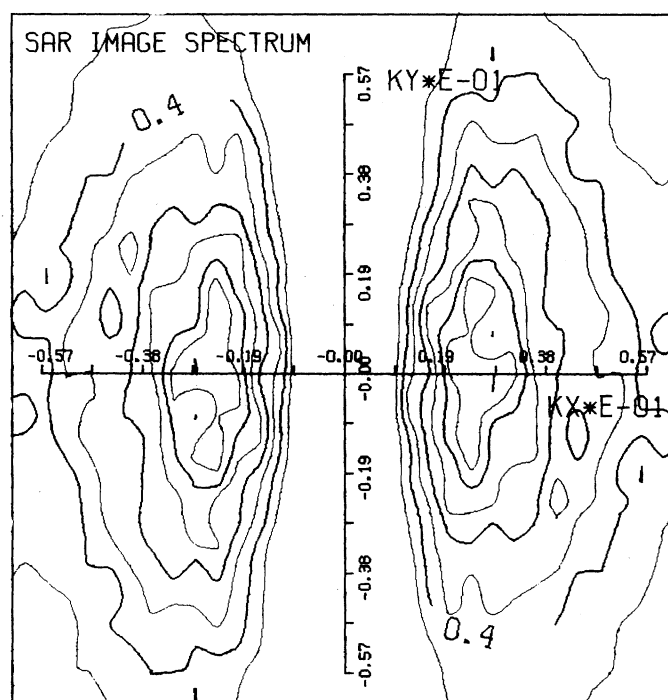
Fig. 3. Computer simulation of Seasat SAR imaging of a fully developed wind sea with peak wavelength of 219 m propagating in flight direction. (a) shows the ocean waveheight spectrum generated by 50 Monte Carlo simulation runs, and (b) the resulting SAR image spectrum that is obtained when applying the complete SAR imaging mechanism. The spectra depicted in (c), (d), (e), (f), and (g) are hypothetical SAR spectra that result when some contributing terms are disregarded in the imaging mechanism. (c), (d), and (e) show the SAR image spectra that result when the degradation of the azimuthal resolution is either completely ignored (c), or partially ignored by neglecting the azimuthal image smear due to the orbital velocity spread within a SAR resolution cell (d), or due to the orbital acceleration arising from the long waves of scale larger than the SAR resolution cell (e). (f) and (g) show the SAR image spectrum that results when linear imaging is assumed (by neglecting velocity bunching and keeping the tilt and hydrodynamic modulation) and when only the azimuthal image smear due to the velocity spread within a SAR resolution cell (f) or the azimuthal image smear due to the orbital acceleration arising from the long waves of scale larger than the SAR resolution cell (g) is active.



(e)



(f)



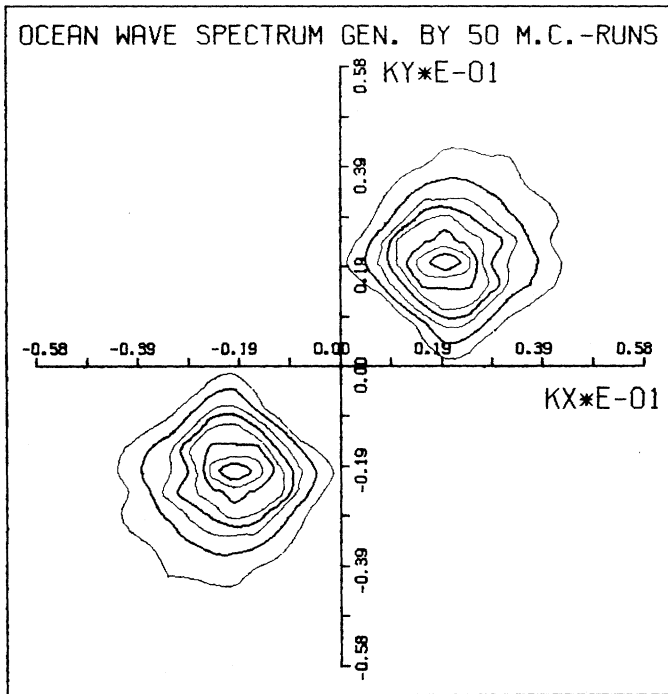
(g)

Fig. 3. (Continued from page 878.)

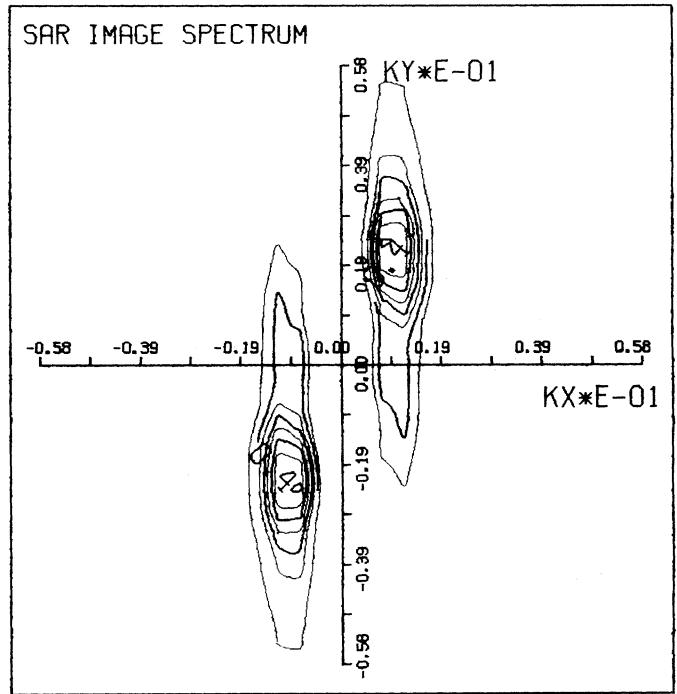
lated SAR image intensity spectra that result when applying the complete SAR imaging mechanism to the ocean waveheight spectra of (a). The other spectra shown in (c), (d), (e), (f), and (g) of Figs. 3 and 4 are hypothetical spectra that are obtained when parts of the motion-related contributions to the SAR imaging mechanism are deleted. All spectra shown in (a)–(g) are normalized to unity at

the spectral peak. The isolines represent the normalized spectral energy density in steps of 0.1 from the peak value 1. All scales in the plots are linear.

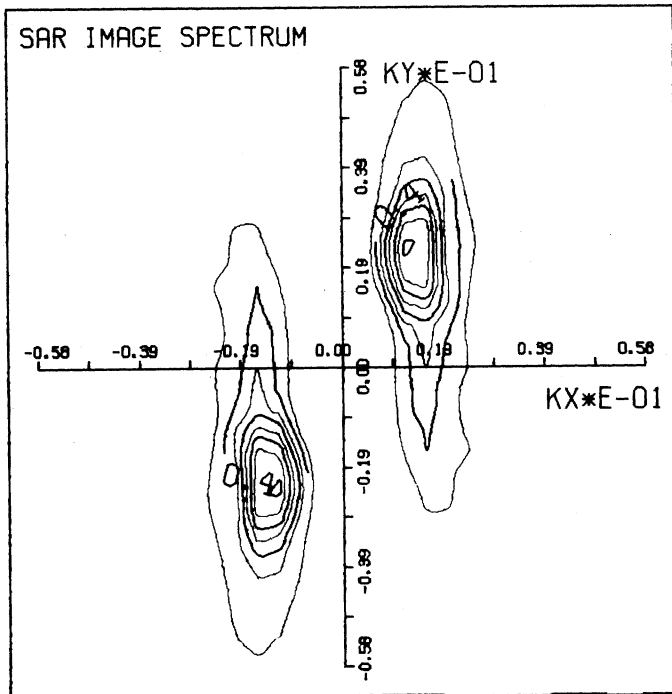
When only velocity bunching is kept in the motion-related part of the imaging mechanism, the spectrum of (c) results. The spectra of (d) and (e) are obtained when, in addition to velocity bunching, the degradation in azimuth-



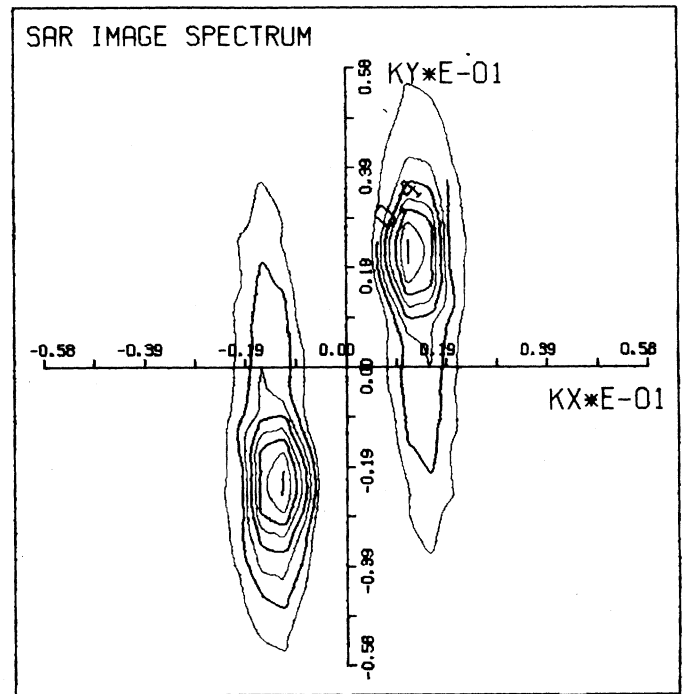
(a)



(b)



(c)



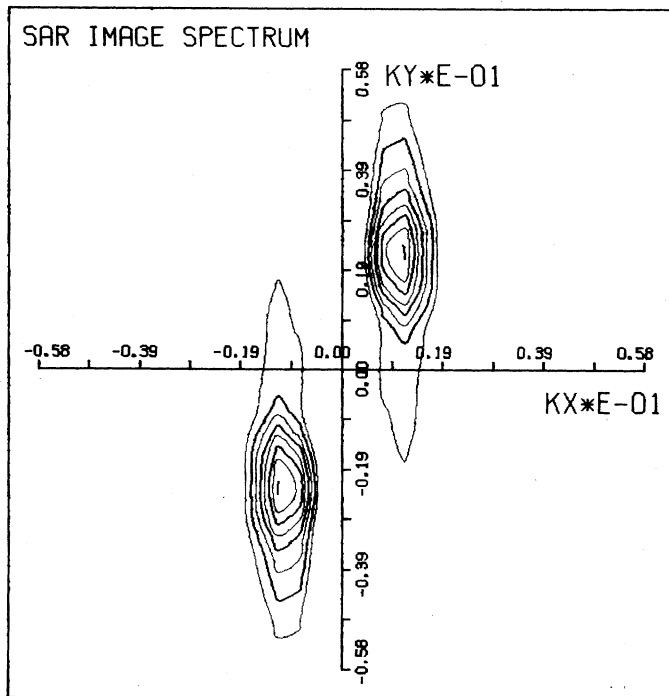
(d)

Fig. 4. Same as Fig. 3, but the propagation direction is 45 degrees to the flight direction.

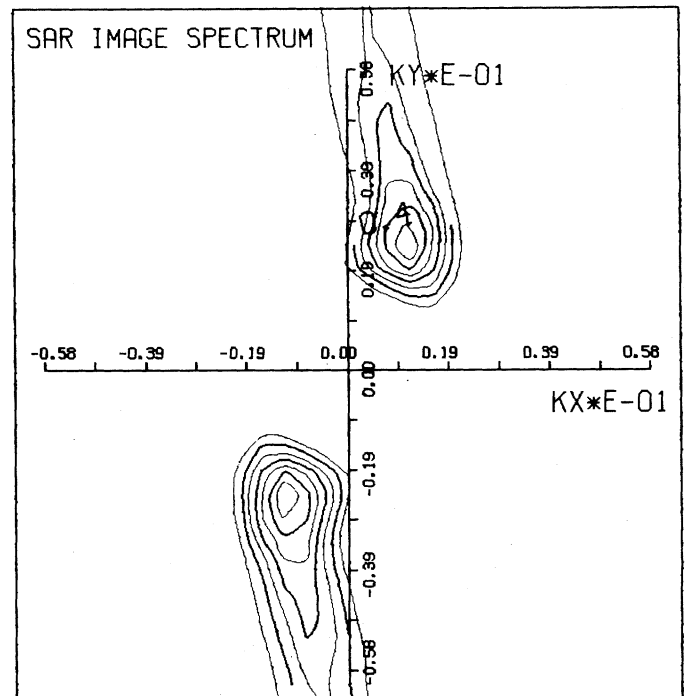
thal resolution is partially included in the imaging mechanism. In the first one, (d), only the degradation due to the orbital accelerations arising from the long waves of scale larger than the SAR resolution cell (as described by $\hat{a}_r(x_0)$ in (2)), are included, and in the second case, (e), only the degradation in azimuthal resolution due to the spread of the radial facet velocities within a SAR resolu-

tion cell (as described by τ_s in (2)). The SAR imaging model leading to the spectrum of (d) is the model used by Alpers [20] in his one-dimensional Monte Carlo simulation study.

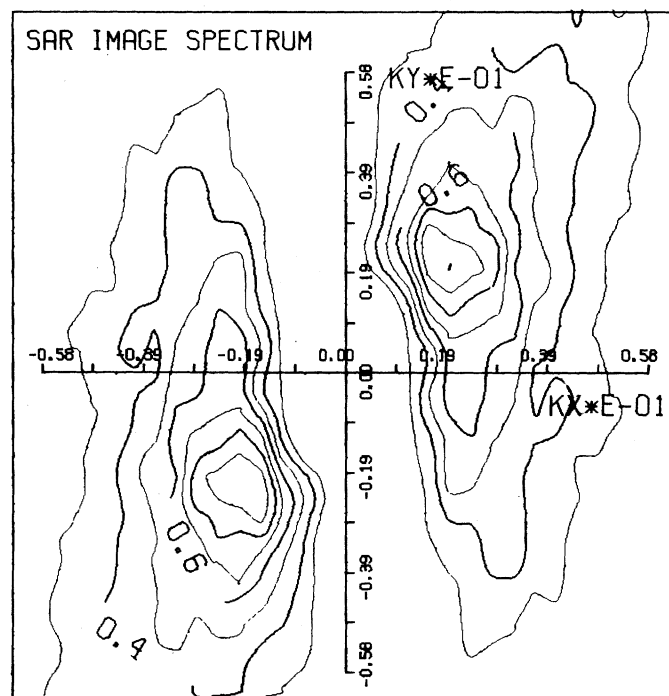
The spectrum of (f) is obtained when velocity bunching and the degradation in azimuthal resolution due to the orbital accelerations arising from the long waves of scale



(e)



(f)



(g)

Fig. 4. (Continued from page 880.)

larger than the SAR resolution cell are ignored (i.e., set equal to zero). In this SAR imaging model the imaging of ocean surface waves is due to the linear tilt and hydrodynamic modulations. The wave motions only affect the imaging by degrading the azimuthal resolution uniformly and thus leading to an azimuthal cutoff of the SAR image intensity spectrum as discussed in [5] and [9].

Finally, the spectrum of (g) is obtained when velocity bunching and the degradation in azimuthal resolution due to the spread of the radial facet velocities within a SAR resolution cell are ignored. Note that the degradation in azimuthal resolution arising from the long waves of scales larger than the SAR resolution cell does not result in an azimuthal low-pass filter.

TABLE I

PEAK WAVELENGTH λ_p AND AZIMUTH ANGLE ϕ

(The values refer to the spectra shown in Figs. 3 and 4. R^{RAR} on, $(\partial/\partial x_0) \hat{u}_r(x_0)$ on, $\hat{a}_r(x_0)$ on, and τ_s on denote that the RAR MTF, velocity-bunching, and degradation in azimuthal resolution due to the orbital accelerations arising from the long waves of scale larger than the SAR resolution cell, and due to the spread of the radial facet velocities within a SAR resolution cell, respectively, are activated in the SAR imaging mechanism.)

	Panel A	Panel B	Panel C	Panel D	Panel E	Panel F	Panel G
ocean	R^{RAR}	R^{RAR} on	R^{RAR} on	R^{RAR} on	R^{RAR} on	R^{RAR} on	R^{RAR} on
waveheight	$\frac{\partial \hat{u}_r(x_0)}{\partial x_0}$ on	$\frac{\partial \hat{u}_r(x_0)}{\partial x_0}$ on	$\frac{\partial \hat{u}_r(x_0)}{\partial x_0}$ on	$\frac{\partial \hat{u}_r(x_0)}{\partial x_0}$ on	$\frac{\partial \hat{u}_r(x_0)}{\partial x_0}$ on	$\frac{\partial \hat{u}_r(x_0)}{\partial x_0}$ off	$\frac{\partial \hat{u}_r(x_0)}{\partial x_0}$ off
spectrum	$\hat{a}_r(x_0)$ on	$\hat{a}_r(x_0)$ off	$\hat{a}_r(x_0)$ on	$\hat{a}_r(x_0)$ on	$\hat{a}_r(x_0)$ off	$\hat{a}_r(x_0)$ on	$\hat{a}_r(x_0)$ on
	τ_s on	τ_s off	τ_s off	τ_s off	τ_s on	τ_s on	τ_s off
imaging model	-	complete	incomplete	incomplete	incomplete	incomplete	incomplete
Fig. 3 λ_p	219 m	571 m	359 m	390 m	496 m	336 m	219 m
ϕ	0°	0°	0°	0°	0°	0°	0°
Fig. 4 λ_p	217 m	243 m	229 m	229 m	229 m	229 m	217 m
ϕ	45°	71.6°	63.4°	63.4°	63.4°	63.4°	45°

In Table I the wavelengths and the directions of the spectral peaks of the various spectra shown in Figs. 3 and 4 are listed. (The spectral peak is defined as the center of the 3-dB line). We have estimated that the rms error originating from the computational technique employed in this study is approximately 5 percent for the peak wavelength and 3 degrees for the rotation angle.

In the example presented in Fig. 3 and Table I the stretching of the peak wavelength from 219 m in the ocean waveheight spectrum to 571 m in the SAR image intensity spectrum is partly caused by the nonlinearity of the velocity bunching mechanism (from 219 to 359 m). However, the degradation in azimuthal resolution due to the finite scene coherence time gives also rise to a stretching of the peak wavelength, which is of the same order of magnitude (from 219 to 336 m). Similar effects are observed in the example shown in Fig. 4, where the waves propagate at 45 degrees to the flight direction.

The same kind of Monte Carlo simulation runs have also been performed for fully developed wind seas of 439-m peak wavelength propagating at 0° and 45° to the flight direction. The results are depicted in Table II. In these examples, the nonlinearity of the velocity bunching is clearly the dominant process causing the stretching of the peak wavelength and the rotation of the spectral peak towards the range direction.

From these and additional Monte Carlo runs not shown in this paper we have obtained the following results:

1) For a fully developed wind sea traveling in azimuth direction, the low-pass filter associated with the degradation in azimuthal resolution due to the spread of the radial facet velocities within a SAR resolution cell can explain only about 60 percent of the stretching of the peak

wavelength by the SAR imaging mechanism when the ocean wave field has a peak wavelength of about 100 m. The effect of the low-pass filter on the stretching decreases with increasing peak wavelength. It is practically absent when the wind sea has a peak wavelength of about 400 m.

2) For fully developed wind seas traveling at angles between 30° and 60° off the azimuth direction, the main effect is the rotation of the peak wave vector into the range direction. If the fully developed wind sea has a peak wavelength of about 100 m, then the rotation of the wave vector of the spectral peak can be explained completely by the azimuthal low-pass filter associated with the degradation in azimuthal resolution due to the spread of the radial facet velocities with a SAR resolution cell. The effect of the azimuthal low-pass filter on the rotation of the wave vector of the spectral peak decreases with increasing peak wavelength.

This statement can be quantified. For that we introduce the nondimensional parameter

$$D = \left[\rho_{aN}^2 + \left(\rho_a \frac{T}{\tau_s} \right)^2 \right]^{1/2} \cdot \lambda_p^{-1} \quad (26)$$

where λ_p is the wavelength of the spectral peak of a fully developed wind sea.

In the case of Seasat SAR imaging our calculations have yielded the following results:

If $D > 2$, the rotation of the spectral peak toward the range direction can be explained almost completely by the low-pass filter whose width is given by the scene coherence time.

If $D < 0.5$, the relative importance of the azimuthal

TABLE II
SAME AS TABLE I, BUT FOR A FULLY DEVELOPED WIND SEA OF PEAK WAVELENGTH 439 m, RESPECTIVELY 434 m, PROPAGATING AT
0° AND 45° TO THE FLIGHT DIRECTION
(The corresponding spectra are not shown.)

	ocean	R $\hat{R} \hat{R}$ on	R $\hat{R} \hat{R}$ on	R $\hat{R} \hat{R}$ on	R $\hat{R} \hat{R}$ on	R $\hat{R} \hat{R}$ on	R $\hat{R} \hat{R}$ on
waveheight		$\frac{\partial}{\partial x} \hat{u}_r(x)$ on	$\frac{\partial}{\partial x} \hat{u}_r(x)$ on	$\frac{\partial}{\partial x} \hat{u}_r(x)$ on	$\frac{\partial}{\partial x} \hat{u}_r(x)$ on	$\frac{\partial}{\partial x} \hat{u}_r(x)$ off	$\frac{\partial}{\partial x} \hat{u}_r(x)$ off
spectrum		$\hat{a}_r(x)$ on	$\hat{a}_r(x)$ off	$\hat{a}_r(x)$ on	$\hat{a}_r(x)$ off	$\hat{a}_r(x)$ off	$\hat{a}_r(x)$ on
		τ_s on	τ_s off	τ_s off	τ_s on	τ_s on	τ_s off
imaging model	-	complete	incomplete	incomplete	incomplete	incomplete	incomplete
λ_p	439 m	687 m	589 m	620 m	643 m	456 m	439
ϕ	0°	0°	0°	0°	0°	0°	0°
λ_p	434 m	480 m	480 m	480 m	480 m	393 m	393 m
ϕ	45°	63.4°	63.4°	63.4°	63.4°	52°	50°

low-pass filter is small with respect to the nonlinearity of the velocity bunching mechanism.

If $0.5 < D < 2$, both mechanisms contribute to the rotation.

The contribution of the azimuthal image smear due to the orbital acceleration arising from the long waves of scale larger than the SAR resolution cell to the stretching of the peak wavelength and the rotation of the spectral peak is small, as evident from Tables I and II. However, the shape of the SAR image spectrum is broadened (g). Therefore, this contribution to the azimuthal image smear is not responsible for the often observed azimuthal fall-off of SAR image spectra.

Another important conclusion that can be drawn from (f) of Figs. 3 and 4 is that linear imaging together with a low-pass filter (which is also a linear imaging element) cannot explain the cigar-like shape often observed in SAR image intensity spectra. In particular, the spectrum shown in (f) of Fig. 3 exhibits a banana-like shape.

V. DISCUSSION AND CONCLUSIONS

Computer simulations of the imaging of fully developed wind seas propagating off-range direction by Seasat SAR show that the stretching of the peak wavelength, the rotation of the wave propagation direction toward the range direction, of the SAR image spectrum cannot always be explained only by the effect of a low-pass azimuthal filter acting on the slope spectrum $|k|^2 P_{\hat{f}}(k)$. However, the often-observed azimuthal cutoff (see, e.g., [4]) seems to be determined mainly by the azimuthal low-pass filter determined by the scene coherence time τ_s .

The nonlinearity of velocity bunching is an important factor for the imaging of wind seas by the SAR's on board Seasat and ERS-1 that cannot be neglected, especially for fully developed wind seas propagating near azimuth di-

rection. The degradation of the azimuthal resolution due to the velocity spread of the scatterers within a resolution cell often can account for a large part of the observed effects, but usually not for all of them. Our calculations indicate that the orbital acceleration arising from the long waves of scale larger than the SAR resolution cell contributes only little to the artifacts observed in SAR imagery of ocean waves. These accelerations depend on the spatial coordinate x_0 and thus do not result in a uniform azimuthal image smear. Therefore, they do not lead to an azimuthal low-pass filter like the spread of the facet velocities within a SAR resolution cell.

In order to define the parameter regions in which the SAR imaging mechanism of wind seas is linear, or weakly or strongly nonlinear, it is not permissible to base the classification only on the degradation in azimuthal resolution. Investigations based on considering only the behavior of the degradation of azimuthal resolutions of ocean wave and radar parameters lead to underestimations of the degree of distortion of the SAR image intensity spectrum [3].

If the degradation of the azimuthal resolution due to the spread of the facet velocities within a resolution cell caused the azimuthal cut-off of SAR image spectra as often stated [5], [6], [9], then this cutoff would be independent of wind speed or waveheight above a certain threshold value, which is obviously not observed [5], [9].

Beal *et al.* [5] report that they found an azimuthal cutoff in SAR image spectra of ocean waves that depends on significant waveheight H_s and R/V through

$$\lambda_c \propto (R/V)(H_s)^{1/2}. \quad (28)$$

Here, λ_c denotes the minimum detectable azimuthal wavelength. For fully developed wind seas with $H_s < 1$ m this dependence can be explained by the low-pass azi-

muthal filter whose width is determined by the scene coherence time and which is given by (20) (see discussion following (15)). According to (13) $H_s < 1$ m corresponds to a wind speed U less than 7 m/s.

However, for fully developed wind seas with $H_s \geq 3.6$ m corresponding to $U \geq 13$ m/s, the width of the azimuthal low-pass filter is independent of waveheight. Therefore, the cut-off wavelength λ_c must be independent of waveheight, too. Thus, if experimental data show that the relationship (28) is valid also for high wave heights, then mechanisms other than the action of the low-pass filter whose width is determined by the scene coherence time as calculated from (20) must be active.

The experimental finding of Valenzuela and Laing [33] that the rms width of the variance spectrum of the Doppler shift f_d of the radar return from the sea surface, which we denote by $\langle (\delta f_d)^2 \rangle$ increases with $H_s^{1/2}$ in the range $1 \text{ m} \leq H_s \leq 8 \text{ m}$, does not explain the dependence of the azimuthal cutoff of Seasat SAR image intensity spectrum on waveheight for wind speeds above 13 m/s. The Doppler spread measured in these experiments originates from large footprints, typically of several hundred meters in diameter, and not from small footprints of the size of the SAR resolution cell. In the experiments of Valenzuela and Laing, the condition $\gamma\rho/U \gg 1$ is fulfilled, where ρ denotes the footprint size of the scatterometer. Therefore, in order to calculate the Doppler spread for these experiments, one has to insert into the expression for the Doppler spread

$$\langle (\delta f_d)^2 \rangle^{1/2} = 2 \lambda_0^{-1} \langle u_r^2 \rangle^{1/2} = 2 \lambda_0^{-1} (V/R) \langle (\delta x)^2 \rangle^{1/2} \quad (29)$$

the right-hand side of (15), which then yields the measured $H_s^{1/2}$ dependence of the Doppler spread.

But for the cases considered in this study, the resolution cell is much smaller. Therefore, (14) applies, not (15). In this case the Doppler spread, and therefore also the azimuthal image smear and the width of the azimuthal filter function $H(k_a)$ (see (7)), are independent of waveheight.

The present study shows further that Seasat SAR imaging of fully developed wind seas cannot be described by a linear imaging process when the waves travel predominantly in flight (azimuth) direction. Thus, in these cases, conventional linear inversion techniques are inapplicable to obtain the waveheight or slope spectrum of the wind waves from the SAR image spectrum. The degree of nonlinearity increases with decreasing peak wavelength and decreasing azimuth angle. The situation is even worse, when SAR imaging of fetch-limited wind seas is considered. Although the width of the spectrum is narrower for fetch-limited wind seas than for fully developed wind seas, the nonlinearity parameter defined in [20] is proportional to the ratio $H_s/\lambda_p^{3/2}$. The ratio is larger for fetch-limited than for fully developed wind seas. This theoretically expected result has been confirmed by further Monte Carlo runs.

It is sometimes stated [34] that highly nonlinear SAR

imaging of ocean surface waves has not been observed in any of the published Seasat data. We suggest that just because of these strong nonlinearities Seasat SAR hardly ever imaged wind waves. However, the situation is different from swell imaging. In this case nonlinearities are much weaker, because the ratio $H_s/\lambda_p^{3/2}$ is smaller for swell than for fully developed wind seas and because the width of a swell spectrum is narrower than the width of a Pierson-Moskowitz spectrum. The fact that the degree of nonlinearity of the SAR imaging mechanism also depends on the width of the ocean wave spectrum has already been pointed out in [20]. Therefore, Seasat SAR imaging of swell can often be described by a linear or weakly nonlinear imaging theory. In this case it often suffices to consider only the effect of the azimuthal low-pass filter to explain the observed distortions of the SAR image spectrum. This is in agreement with statements made by Beal *et al.* [5], [9], [34].

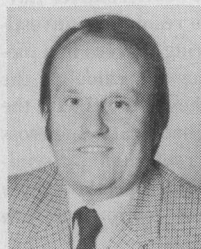
Finally, we note that the results presented in this paper, which have been derived with the Seasat SAR parameters inserted, would have turned out almost the same with ERS-1 SAR parameters inserted, since the R/V ratio and the geometric resolutions for both systems are almost the same [27], [28].

REFERENCES

- [1] W. M. Brown and L. J. Porcello, "An introduction to synthetic aperture radar," *IEEE Spectrum*, vol. 6, pp. 57-62, 1969.
- [2] R. O. Harger, *Synthetic Aperture Radar Systems*. New York: Academic, 1970.
- [3] K. Hasselmann, R. K. Raney, W. J. Plant, W. Alpers, R. A. Shuchman, D. R. Lyzenga, C. L. Rufenach, and M. J. Tucker, "Theory of SAR ocean wave imaging: the MARSEN view," *J. Geophys. Res.*, vol. 90, pp. 4659-4686, 1985.
- [4] H. Seichter, "Two-dimensional power spectra of Seasat SAR imagery," Workshop on SAR image quality, Frascati, Italy, Dec. 11-12, 1980, ESA Pub. SP-172, pp. 55-58, 1980.
- [5] R. C. Beal, D. G. Tilley, and F. M. Monaldo, "Large- and small-scale spatial evolution of digitally processed ocean wave spectra from Seasat synthetic aperture radar," *J. Geophys. Res.*, vol. 88, no. C7, pp. 1761-1778, 1983.
- [6] D. R. Lyzenga and R. A. Shuchman, "Analysis of scatterer motion effects in MARSEN X-band SAR imagery," *J. Geophys. Res.*, vol. 88, no. C14, pp. 9769-9775, 1983.
- [7] R. A. Shuchman, W. L. Rosenthal, J. D. Lyden, D. R. Lyzenga, E. S. Kasischke, H. Guenther, and H. Linne, "Analysis of MARSEN X-band ocean wave data," *J. Geophys. Res.*, vol. 88, no. C14, pp. 9757-9768, 1983.
- [8] J. F. Vesecky and R. H. Stewart, "The observation of ocean surface phenomena using imagery from the Seasat synthetic aperture radar—An assessment," *J. Geophys. Res.*, vol. 87, pp. 3397-3430, 1982.
- [9] F. Monaldo, "Improvement in the estimation of dominate wavenumber and direction from spaceborne SAR image spectra when corrected for ocean surface movement," *IEEE Trans. Geosci. Remote Sensing*, vol. GE-22, no. 6, pp. 603-608, 1984.
- [10] C. E. Elachi and W. E. Brown, "Models of radar imagery of ocean surface waves," *IEEE Trans. Antennas Propagat.*, vol. AP-25, pp. 84-95, 1977.
- [11] W. A. Alpers and C. L. Rufenach, "The effect of orbital motions on synthetic aperture radar imaging of ocean waves," *IEEE Trans. Antennas Propagat.*, vol. AP-27, pp. 685-690, 1979.
- [12] C. T. Swift and L. R. Wilson, "Synthetic aperture radar imaging of ocean waves," *IEEE Trans. Antennas Propagat.*, vol. AP-27, pp. 725-729, 1979.
- [13] G. R. Valenzuela, "An asymptotic formulation for SAR images of the dynamical ocean surface," *Radar Sci.*, vol. 15, pp. 104-114, 1980.

- [14] R. K. Raney, "SAR response to partially coherent phenomena," *IEEE Trans. Antennas Propagat.*, vol. AP-28, pp. 777-787, 1980.
- [15] R. O. Harger, "The synthetic aperture radar image of time variant scenes," *Radio Sci.*, vol. 15, pp. 749-759, 1980.
- [16] C. L. Rufenach and W. A. Alpers, "Imaging ocean waves by synthetic aperture radars with long integration times," *IEEE Trans. Antennas Propagat.*, vol. AP-29, pp. 422-428, 1981.
- [17] R. K. Raney, "Wave orbital velocity, fade and SAR response to azimuth waves," *IEEE J. Oceanic Eng.*, vol. OE-6, pp. 140-146, 1981.
- [18] A. Jain, "SAR imaging of ocean waves: Theory," *IEEE J. Oceanic Eng.*, vol. OE-6, pp. 130-139, 1981.
- [19] W. R. Alpers, D. B. Ross, and C. L. Rufenach, "On the detectability of ocean surface waves by real and synthetic aperture radar," *J. Geophys. Res.*, vol. 86, pp. 6481-6498, 1981.
- [20] W. R. Alpers, "Monte Carlo simulations for studying the relationship between ocean wave and synthetic aperture radar image spectra," *J. Geophys. Res.*, vol. 88, no. C3, pp. 1745-1759, 1983.
- [21] —, "Imaging ocean surface waves by synthetic aperture radar—A review," in *Satellite Microwave Remote Sensing*, T. D. Allan, Ed. Chichester, England: Ellis Horwood Limited, 1983, ch. 6.
- [22] S. Rotherham, "Theory of SAR ocean wave imaging," *Satellite Microwave Remote Sensing*, T. D. Allan, Ed. Chichester, England: Ellis Horwood Limited, 1983, ch. 10.
- [23] W. J. Plant and W. C. Keller, "The two-scale wave probe and SAR imagery of the ocean," *J. Geophys. Res.*, vol. 88, no. C14, pp. 9776-9784, 1983.
- [24] A. V. Ivanov, "On the mechanism for imaging ocean waves by synthetic aperture radar," *IEEE Trans. Antennas Propagat.*, vol. AP-31, pp. 538-541, 1983.
- [25] M. J. Tucker, "The imaging of waves by satelliteborne synthetic aperture radar: The effects of sea surface motion," *Int. J. Remote Sensing*, vol. 6, pp. 1059-1074, 1985.
- [26] D. R. Lyzenga, R. A. Shuchman, J. D. Lyden, and C. L. Rufenach, "SAR imaging of waves in water and ice: Evidence of velocity bunching," *J. Geophys. Res.*, vol. 90, no. C1, pp. 1031-1036, 1985.
- [27] R. L. Jordan, "The Seasat-A synthetic aperture radar system," *IEEE J. Oceanic Eng.*, vol. OE-5, pp. 154-164, 1980.
- [28] F. G. Sawyer, P. R. Cox, and H. Joyce, "ERS synthetic aperture radar design," in *Proc. 1984 Int. Geosci. Remote Sensing Symp. (IGARSS' 1984)*, (Strasbourg, Aug. 27-30, 1984), European Space Agency, ESA SP-215, pp. 827-832, 1984.
- [29] R. K. Raney, "SAR processing of partially coherent phenomena," *Int. J. Remote Sensing*, vol. 1, no. 1, pp. 29-51, 1980.
- [30] O. M. Phillips, *The Dynamics of the Upper Ocean*. New York: Cambridge University Press, 1977.
- [31] M. J. Tucker, "The decorrelation time of microwave echoes from the sea surface," *Int. J. Remote Sensing*, vol. 6, pp. 1075-1089, 1985.
- [32] H. Mitsuyasu, F. Tasai, T. Suhara, S. Mizuno, M. Ohkusu, T. Honda, and K. Rikiishi, "Observations of directional spectrum of ocean waves using a cloverleaf buoy," *J. Phys. Oceanography*, vol. 5, pp. 750-760, 1975.
- [33] G. R. Valenzuela and M. B. Laing, "Study of Doppler spectra of radar sea echo," *J. Geophys. Res.*, vol. 75, pp. 551-559, 1970.
- [34] R. C. Beal, F. M. Monaldo, D. G. Tilley, D. E. Irvine, E. J. Walsh, F. C. Jackson, D. W. Hancock, D. E. Hines, R. N. Swift, F. I. Gonzalez, D. R. Lyzenga, and L. F. Zambresky, "A comparison of SIR-B directional ocean wave spectra with aircraft scanning radar spectra," *Science*, vol. 232, pp. 1531-1535, 1986.

*



Werner R. Alpers was born on Aug. 26, 1936 in Hamburg, Germany. He studied physics at the Universities of Hamburg, Zurich, and Wisconsin. He received the diploma in physics (Dipl.-Phys.) from the University of Hamburg, Hamburg, Germany, in 1962, the M.S. degree in physics from the University of Wisconsin, Madison, in 1964, and the Ph.D. degree (Dr. rer. nat.) in theoretical physics (elementary particle physics) from the University of Hamburg, in 1967.

From 1968 to 1970 he worked in space physics at the European Space Research Institute at Frascati, Italy, and from 1970 to 1973 at the Max-Planck-Institute for Physics and Astrophysics in Munich, Germany. From 1973 to 1985 he was with the University of Hamburg and the Max-Planck-Institute for Meteorology in Hamburg, Germany, working on radio oceanographic research problems. Since Feb. 1, 1985 he has been professor for physical oceanography in the Department of Physics and Electrical Engineering at the University of Bremen, Bremen, Germany. His current research activities are focused on microwave remote sensing of the ocean by using laboratory, air-borne, and space-borne sensors.

*



Claus Bruening was born in Bremerhaven, Germany, on Feb. 12, 1953. He received the diploma degree in meteorology from the University of Hamburg, Hamburg, Germany, in 1982. Since 1982 he has been at the Max-Planck-Institute for Meteorology in Hamburg working for the Ph.D. degree in oceanography.

His main research interests in remote sensing are theoretical SAR simulation studies of ocean waves.